Revised: February 28, 2016

Investigating the stability of a laser-based plasma x-ray source

Fredrik Parnefjord Gustafsson

Thesis submitted for the degree of Bachelor of Science

LUND UNIVERSITY

Department of Physics

Department of Chemical Physics, Lund University

Project duration: 2 months
Date of the examination: 27 May 2015
Supervised by Jens Uhlig

Abstract

The use of laser based plasma x-ray sources (LPXS) has quickly expanded during the past decades due to rapid development of ultrafast laser systems. These sources are used in many research applications such as emission, absorption and particularly time-resolved spectroscopy. From the LPXS x-ray pulses are generated when an intense laser pulse is focused onto a liquid or solid interface in gas or vacuum. In this thesis we investigate the source stability which we define as the x-ray flux and spectrum reproducibility from each generated x-ray pulse. Understanding the stability is of great importance for its research applications. A basic theory of the LPXS is introduced describing relevant parameters for the source stability. Two parameters of relevance for the LPXS stability were investigated: The laser pointing and pulse energy fluctuations. These were experimentally determined using a beam profiler, capturing the beam profile of each laser pulse at 1 kHz. The relevance of these parameter fluctuations to the source stability is discussed based on these measurements. An existing LPXS setup was reconstructed in preparation for shot to shot stability measurements. A synchronized chopper system was built to decrease the laser pulse frequency for single pulsed mode and a program was developed for analyzing the x-ray photons captured by an x-ray CCD camera. Problems with the laser system prevented successful gathering of data within the time of the project. Future measurements based on these preparations will reveal the stability of the LPXS.

Contents

Acronyms

ATI Above-Threashold Ionization. 2

CCD Charge-Coupled Device. 13

CPA Chirped Pulse Amplification. 1, 10

LPXS Laser Plasma X-ray Source. 1, 2

MPI Multiphoton Ionization. 2

TES Transition Edge Sensors. 1, 13

TI Tunneling Ionisation. 3

1 Introduction

The performance of laser systems has quickly developed during recent decades[3, 5, 2]. Table top laser systems are now capable of reaching peak intensities higher than TW/cm^2. One often used approach to reach these intensities is Chirped Pulse Amplification (CPA), which temporally expands the laser pulse before amplifying it and re-compressing. The use of this technique combined with the rapid development of solid-state lasers[3, 2] has opened the door to the commercialization of high power laser systems around the world. As a result this allows for the construction of laser x-ray sources such as high harmonics generation, laser wakefield acceleration, laser driven x-ray diodes and the Laser Plasma X-ray Source (LPXS)[5] which will be investigated in this report. The LPXS works by focusing an intense laser pulse onto a target water-jet. When the laser pulse interacts with the water surface, the strong laser field ionizes the target and accelerates the electrons into the water surface. The deceleration of electrons results in the emission of x-rays with energies of a few keV[3, 1] and characteristic radiation with emission lines from oxygen. The electron acceleration time is limited to the passage of the laser pulse, thus the generated broadband x-ray pulse is well defined in time and well suited for time-resolved spectroscopy measurements[5]. In combination with the LPXS an advanced superconducting microcalorimeter is used to detect individual x-ray photons with an accuracy of < 5 eV for photon energies up to $\approx$10 keV[22]. This detector uses a number of superconducting Transition Edge Sensors (TES) in an array matrix for single photon counting and measuring of photon energies. The array of sensors makes it possible to capture the broadband spectrum for each individual x-ray pulse. The LPXS combined with the TES microcalorimeter makes it possible to both generate and analyze broadband x-ray spectra for spectroscopic measurements[6]. These experiments often require as many as 10^7 x-ray pulses to collect sufficient statistics for the resulting spectrum. Understanding the pulse to pulse x-ray flux and spectrum fluctuations are thus of great importance to justify the averaging of spectra. The motivation for this thesis is to obtain a greater understanding of the stability (spectrum and x-ray flux reproducibility) of the LPXS. The origins of the x-ray pulse to pulse fluctuations from the LPXS are therefore investigated. Crucial for the stable production of x-rays is the relative position of the repeatedly changing target with respect to the laser focal point. A water-jet is used as a replaceable target for laser pulses with a 1 kHz repetition frequency. The water-jet fluctuations will be discussed but not determined in this report. Two important sources of source fluctuation will be investigated: The laser pointing and the pulse energy fluctuations. These measurements are performed in preparation for more extensive pulse to pulse measurements of the x-ray flux and spectrum. The approach and necessary preparation for these measurements will be described in this thesis. When the shot to shot experiments are performed the prediction based on the external sources of fluctuation can be verified. An advanced understanding of the stability of the LPXS and the sources of fluctuation will help to improve the design for future versions of similar setups. This research is consequently significant for the ongoing development of laser plasma x-ray sources.

1.1 Background

Methods of generating x-rays has been known since its discovery in the late 19th century by Wilhelm Röntgen[12]. X-rays are invisible electromagnetic waves of higher energy than visible light with a wavelength of 0.01 to 10 nanometers[12]. They were originally produced by applying a high voltage potential between two plates in a vacuum tube; electrons were accelerated in the electric field until decelerated through direct and indirect collisions. The high energy electrons release their kinetic energy in the form of x-radiation called bremsstrahlung, due to the electron deceleration. This invisible radiation is capable of passing though solid matter and producing images on fluorescent screens and photographic plates[12]. Transitions from the outer higher energy levels to the inner core will emit an x-ray photon with a discrete energy, the opposite transition can occur for the absorption of a photon as long as the receiving state is empty. In x-ray emission and absorption spectroscopy characteristic x-radiation is used to obtain information about the atomic energy states[23]. This is one of many valuable uses for the x-rays generated by the LPXS. The sequence of events leading to the x-ray generation from the LPXS will be described in the coming sections. A perspective of necessary conditions for the generation of x-rays will be relevant for the understanding of the parameters affecting the stability of the LPXS.

1.1.1 Plasma formation

Consider a high intensity laser pulse of 800 nm wavelength focused on a flowing cylindrical water-jet target. The moment the leading edge of the laser pulse reaches the water, light-matter interactions will start to occur. The light package can be observed either in a wave or particle picture. In the particle picture the pulse consists of a highly dense photon bunch with an average photon energy of 1.38 eV. According to the Einstein model of the single-photon photoelectric effect, the low energy photons do not have sufficient energy to cause ionization at the water surface. However, interesting behaviors start to occur at these high laser intensities, such as multiphoton processes. Many models have been developed in order to understand the behavior in different intensity regimes[2, 1]. According to the Heisenberg uncertainty principle, $\Delta E \Delta t \leq \hbar$ where ΔE is the energy uncertainty for a state and Δt is the lifetime of the state. For a virtual state the energy uncertainty is very high which leads to a very short lifetime. If a second photon arrives within the lifetime of the virtual state there is a probability for double or even multiphoton absorption[5]. This is a much simplified picture and in reality the process is much more complicated[24]. At high laser intensities multiphoton absorption into previously inaccessible states can occur, resulting in Multiphoton Ionization (MPI). Indeed even more photons can be absorbed than what is needed for ionization, this is called Above-Threashold Ionization (ATI), see figure 1. In this case the electron kinetic energy K can be described by the extended Einstein formula[1],

$$K = (n + s)\hbar\omega - \phi_{ion};$$

where n is the number of photons absorbed for above threshold multiphoton excitation, s is the additional photons absorbed and ϕ_{ion} is the ionization energy. The ATI results in electrons with significant momentum leaving the atomic potential.

In order to estimate the field strength needed for ionization one can compare with the electric field strength within the atomic potential[1],

$$E_a = \frac{e}{4\pi\epsilon_0 a_B^2} \approx 5.1 \cdot 10^9 \text{ V/m}.$$

In this expression a_B is the Bohr radius, e is the electron charge and ϵ_0 is the dielectric constant in vacuum. This corresponds to a field intensity of about $I_a = \frac{\epsilon_0 c E_a^2}{2} \approx 3.51 \cdot 10^{16}$ W/cm^2. When the field intensity is greater than this order of magnitude it will affect the shape of the coulomb potential. The MPI theory assumes an undisturbed atomic potential. In very strong laser fields where the electric field component E_L is greater than E_a the potential will no longer remain undisturbed. The coulombic field term combines with the electric field term to create an effective potential[1]:

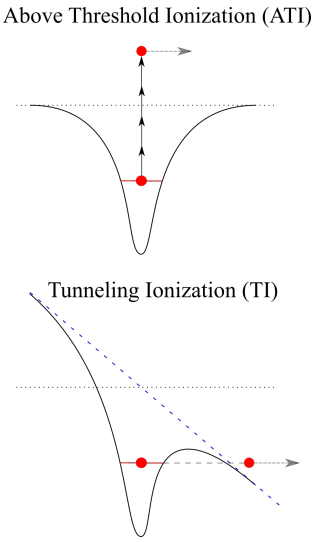

Figure 1: Schematics of ATI and TI.

$$V(x) = -\frac{Ze^2}{4\pi\epsilon_0|x|} - eE_L x$$

here $-\frac{Ze^2}{4\pi\epsilon_0|x|}$ is the coulomb potential and $-eE_L x$ is the electric field potential. The electric field will tilt the potential such that only a small barrier is left which the electrons can tunnel through. This process is called Tunneling Ionisation (TI), see figure 1. The electrons leaving the potential can be accelerated by the electric field until the field direction changes, the electron will either leave the atomic potential or might reenter the potential transferring energy to a core electron which can cause further ionization.

Both ionization processes will result in the formation of a plasma at the interaction point. The excess energy obtained by the electrons through the ionization process will result in heating of the plasma. When the rest of the pulse train enters the plasma new forms of interactions will occur which leads us to the next subsection describing the laser plasma interaction.

1.1.2 Laser plasma interaction

The ionization caused by the initial interaction with the laser pulse has generated a zone of strongly inhomogeneous plasma at the water surface. The free electrons in the plasma will have a resonance frequency as a function of the electron density n_e called the plasma frequency ω_p,

$$\omega_p = \sqrt{\frac{e^2 n_e}{\epsilon_0 m_e}}.$$

At this resonance frequency the energy transfer from the driving field to the electron oscillation is maximized. When the laser pulse reaches the critical electron density n_c (where the plasma frequency equals the laser frequency) the plasma acts as a mirror, reflecting any incoming light. A plasma gradient will behave as a refractive gradient up

to this point, see figure 2. When the density is lower the plasma is called underdense and for higher density, overdense. The refraction index can be calculated[3],

$$n = \sqrt{1 - \frac{n_e}{n_c}} \text{ or } n = \sqrt{1 - \frac{\omega_p^2}{\omega_L^2}}.$$

Regions of higher electron density will give a lower refractive index and vice versa. At the focal spot the ionization and the electron density is higher due to the higher laser intensity (resulting in greater ionization and therefore a higher electron density). This causes a defocusing effect at the laser focal point[5, 1].

A plasma gradient is quickly formed by the first few laser cycles reaching the water surface, the steepness of this gradient determines the size of the plasma interaction region.

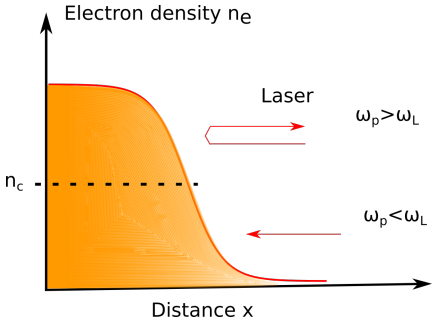

Figure 2: Plasma gradient formed by the laser interacting with the target surface. The laser will propagate until the critical density n_c is reached.

The region of ions in the plasma will expand by ablation from the plasma pressure with a velocity in the order of the speed of sound c_s (while the electrons move with a much higher velocity). For short femtosecond pulses this ion plasma region will have very little time to expand before the peak of the laser pulse envelope arrives. The plasma plume will thus present a scale-length given by $L = c_s \tau_L$ where τ_L is the laser pulse duration[1]. For very short and intense pulses used in our experiment the scale length can be roughly calculated assuming $c_s = 300$ m/s and a pulse duration of $\tau_L = 4 \cdot 10^{-14}$ s, this gives a scale length of $L = 1.2 \cdot 10^{-11}$ m; comparing to a wavelength of $\lambda = 800$ nm gives $L/\lambda \approx 1 \cdot 10^{-5}$. This is a very steep gradient that can be well approximated by a Heaviside step function. The laser field results in a very high degree of ionization at this region, thus the pulse envelope will interact almost directly with the critical electron density. The incoming laser pulse will form a standing wave pattern at the mirror-like plasma surface, combined with a component that penetrates into the overdense plasma region. The penetrating component will have a characteristic skin depth given by $l_s = c/\omega_p$[1]. A plane polarized pulse will couple strongly to electrostatic plasma modes if the electric field component is parallel to the surface normal along with the electron density gradient. The electric field can resonantly drive plasma waves around the critical density to increasing amplitude. This is a collisionless absorption process where electrons can reach energies far beyond the thermal energies of the plasma. These superthermal electrons are called hot electrons. For gentle density gradients the plasma waves can be solved for using the Wentzel-Kramers-Brillouin (WKB) approximation but unfortunately this approximation fails at the steeper gradients. Instead numerical methods are often used[1]. In the optimal case, a well defined short pulse creates a plasma with a small scale-length as previously calculated. The situation $L \to 0$ corresponds to the density gradient resembling a Heaviside step function. For strong electric fields the thermal electrons close to the plasma edge can gain enough kinetic energy from the electric field that they can leave the plasma and enter the vacuum where

they are at the mercy of the strong laser field. This is called vacuum heating and is described by the so called Brunel mechanism[17, 1]. Consider an incoming horizontally polarized laser pulse incident at the angle θ on this steep plasma gradient, see figure 3. The reflection will create a standing wave at the surface generating the effective driving electric field perpendicular to the surface:

$$E_d = 2E_L sin(\theta). \tag{1.1}$$

In this equation we assume that the electric field E_L of the reflected beam and the incident beam is the same, which is not entirely true due to absorption but will be assumed for simplicity for now. This effective electric field will pull out a cloud of electrons to a distance Δx from the plasma. This charge separation will generate an electric field opposing the driving electric field. This electric field between $x = 0$ and $x = -\Delta x$ assuming an electron density n_e is easily derived in analogy with a plane plate capacitor and is given by

$$\Delta E = 4\pi e\sigma,$$

where $\sigma = n_e \Delta x$ is the surface density and e is the elementary charge. The electron cloud will be pulled out until equilibrium is reached, $\Delta E = E_d$ this implies that the surface density is

$$\sigma = \frac{E_d}{4\pi e} = \frac{E_L \sin(\theta)}{2\pi e}. \tag{1.2}$$

When the phase of the laser light changes the two electric field components will be parallel and the cloud of electrons will accelerate back into the plasma. When the electron reaches the charge equilibrium in the plasma, the electron cloud will have acquired a velocity $v_d \approx 2v_q \sin(\theta)$ where v_q is the electron quiver velocity in the laser field; for linearly polarized light it is given by $v_q = \frac{eE_L}{m_e\omega}$. The electrons reentering the plasma with a high kinetic energy will continue through the target beyond the skin depth where the electric field no longer has effect. The average energy density per laser cycle for the electrons is given by

$$P_a = \frac{\sigma}{\tau}\frac{m_e v_d^2}{2},$$

where $\tau = \frac{2\pi}{\omega}$ is the time for one laser cycle and m_e is the electron mass[1]. Inserting the expression for the quiver velocity combined with equation 1.1 and 1.2 gives[1]:

$$P_a \approx \frac{eE_d^3}{16\pi m_e \omega}.$$

This expression can be compared to the laser intensity given by the averaged Poynting vector $P_L = \frac{cE_L^2}{8\pi}\cos(\theta)$, hence the fraction of the absorbed intensity is

$$\eta = P_a/P_L = a\frac{4\sin^3(\theta)}{\pi\cos(\theta)}.$$

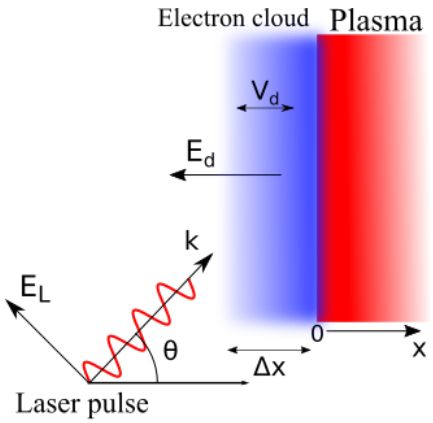

Figure 3: Model of the vacuum heating process.

In this equation a is the ratio between the quiver velocity and the speed of light c; $a = v_q/c$. This is sometimes called the normalized vector potential and can be greater than 1 in the relativistic regime where $v_{qrel} = \gamma v_q$[16]. In our case we are dealing with a laser intensity of 10^{18} W/cm^2 at 800 nm where $a \approx 1$, which is in the weak relativistic regime. The approximate expression gives an indication of the angular dependence of the laser absorption; higher absorption is seen at greater angles. Moreover the absorption exceeds 100%, corrections are required. At first we have assumed that the reflected beam has the same intensity as the incoming, which is apparently not the case. Due to the absorption of the laser light the driving electric field will no longer be given by 1.1 but instead $E_d = fE_L sin(\theta)$ where $f = 1 + (1-\eta)^{1/2}$. Since we are dealing with relativistic electrons we exchange the classical kinetic energy in equation 1.2 with the relativistic kinetic energy. Combining these two corrections and after some algebra the following expression is revealed:

$$\eta_C = f[(1 + f^2 a^2 \sin^2(\theta))^{1/2} - 1]\frac{\tan(\theta)}{\pi a} \tag{1.3}$$

which was originally described by Brunel[17]. This expression describes the angular dependence of the fractional absorption into the vacuum heating process. But since f is a function of η we end up with a nonlinear system of two equations. This system is solved numerically. The absorption reaches 100% which does not reflect reality, an absorption factor C is therefore multiplied with the fractional absorption to correct for energy losses through other processes, such that $f = 1+(1-C\eta)^{1/2}$. Solution to equation 1.3 for different values of C can be seen in figure 4. This shows the angular dependence of the vacuum heating process with an angle of maximum absorption varying from 82° assuming 100% absorption to about 68° for $C = 3$. We have so far assumed non-mobile ions, in reality an ion shelf will be pulled along with the electron cloud after a few laser cycles, decreasing the steepness of the density gradient. We also neglect the magnetic field, complicated Lorentz forces will prevent the electrons from a straight trajectory back through the plasma. Despite these assumptions the theory describes the main components necessary for the generation of hot electrons.

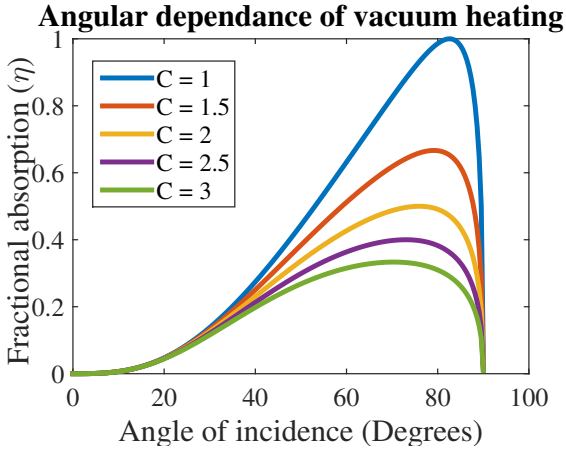

Figure 4: The solutions for the angular dependence of the vacuum heating process for different absorption factors C. The point of maximum absorption vary from 82° ($C = 1$) to 68° ($C = 3$).

1.1.3 X-ray generation

So far we have assumed a plane wave with infinite extension incident on a flat target. In reality the interaction point is finite at the focal point on our water-jet. The approximate size of the focal point is given from Rayleigh theory assuming a Gaussian beam: $D \approx \frac{4\lambda}{\pi\theta_{div}}$ where D is the beam waist diameter, θ_{div} is the total angular spread and λ is the wavelength. In the setup used, we have an approximate beam divergence of 0.4 radians and a wavelength of 800 nm resulting in a beam diameter of about 2.5 μm. The interaction spot size on the water target will be slightly greater than this due to the projection on the tilted water-jet surface. The hot electrons accelerated through the vacuum heating process at the laser spot will be attenuated within the water target. Simulation[1] showed an attenuation length of around 2 μm into the water target and an interaction region of about 4 μm in diameter, see figure 5. The deceleration of the electrons will give rise to bremsstrahlung with a Maxwellian distribution up to energies of about 10-15 keV[5] in the full 4π solid angle from this source region. The strongly diverging pulse of x-rays generated at the target is only present during the laser pulse interaction time which is around tens of femtoseconds. Experimental samples of generated source emission spectra can be seen in figure 6 for varying pulse energies. In addition to the hot electron bremsstrahlung there are other features which contribute to the resulting source emission spectrum. A broadband feature arises from the black body radiation generated by the plasma. This feature usually has an energy below 1 keV[3], due to the thermalisation time of the plasma this radiation persists longer than the laser pulse interaction time[3]. It is rarely of significance due to the short attenuation length of the low energy x-rays. Another feature is the characteristic line radiation. The ionization and recombination of the target material will generate characteristic line radiation depending on the material used. In the case of a water target oxygen K_α lines are generated in the soft x-ray regime. However, this energy is often too low to pass the material in between the source and detector.

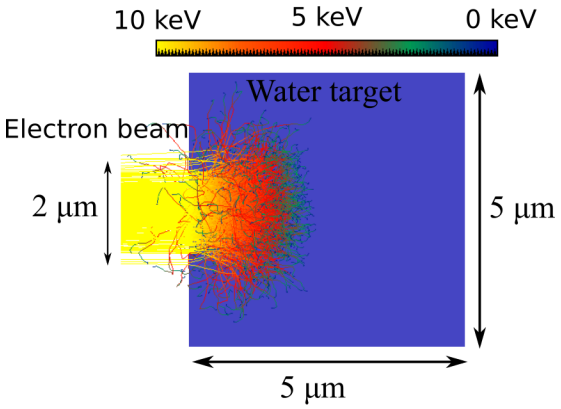

Figure 5: Simulation of a 10 keV electron beam into the water target using CASINO Monte Carlo simulator.

The resulting characteristic broadband spectra generated from the LPXS, as seen in figure 6, can be used for various spectroscopy measurements[3, 5, 11]. When performing these measurements only the linear regime between ≈6-10 keV is used. The LPXS successfully has to reproduce this spectrum with a constant slope each time the laser pulse interacts with the target. Due to the relatively low x-ray flux generated by each pulse, as many as 10^7 pulses are often needed to generate a complete spectrum[22]. The

[1]The electron attenuation was investigated using a simulator called CASINO - (monte CArlo SImulation of electroNs in sOlids). We assumed an electron beam at a typical energy observed from experiments of 10 keV[5] and a 2 μm beam width.

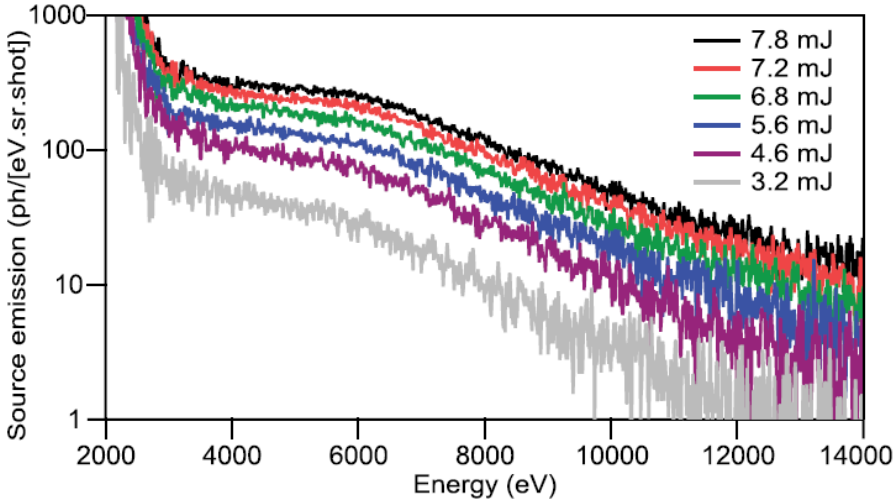

Figure 6: Emission spectra from an LPXS for different laser pulse energies.[11]

source stability which we define as the flux and spectrum variability between shots from the LPXS is therefore of great importance for experiments. Understanding the relevant parameters affecting source stability is necessary for performing accurate spectroscopic measurements using the LXPS. One relevant parameter affecting the x-ray generation is the laser intensity. The laser intensity is a function of average pulse power and laser spot size. The laser pulse power is in turn proportional to the pulse energy. Variation in the pulse energy results in changed conditions for the x-ray generation as seen in figure 6. The spectrum shape is dependent on the hot electron temperature T, which scales as[11]

$$T \propto (I\lambda^2)^{\alpha}, \tag{1.4}$$

where I is the laser intensity and λ is the wavelength. The exponent α varies greatly with respect to many different parameters such as pulse duration and shape[5, 3, 1]. Measurements done on a similar LPXS suggests $\alpha \approx 0.3$[11]. Any fluctuations in laser energy will result in a changed x-ray flux and a varied slope in the fitted region, which is highly undesirable. Finding and reducing fluctuations in laser intensity is of importance for improving the stability of the source.

Since we are dealing with a cylindrical water-jet target any movement of the laser focal spot relative to the target surface will result in a changed x-ray generation due to the angular dependence of the vacuum heating process. A slightly changed horizontal laser position will result in a different laser-target angle,

$$\theta = \arcsin\left(1 - \frac{2b}{d}\right) \tag{1.5}$$

where b is the horizontal translation from the cylinder axis and d is the water-jet diameter see figure 7. The dependence of the x-ray intensity with respect to transverse laser position[2] can be seen in figure 7. The two peaks correspond to the sides of the

[2]In order to investigate the dependence of laser position to the x-ray intensity a water-jet target scan was performed. The laser was moved along the ≈200 μm water-jet axis b as seen in figure 7, meanwhile an x-ray detector (Andor CCD, described in section 2.3) placed at the side of the water-jet was used to capture the integrated x-ray intensity at different positions.

water-jet where the laser is incident at a greater angle as previously described by the vacuum heating theory and seen in figure 4. Since the detector was placed on one side of the jet the peak heights are different. This is due to the x-rays being attenuated through the water on the way to the detector. A comparison between the theoretical vacuum heating model and the experimental data can be seen in appendix B which verifies the accuracy of the vacuum heating model. For optimal performance the laser should positioned at the peak yielding maximum x-ray intensity. Any transverse motion along the jet will result in changed x-ray intensity accordingly.

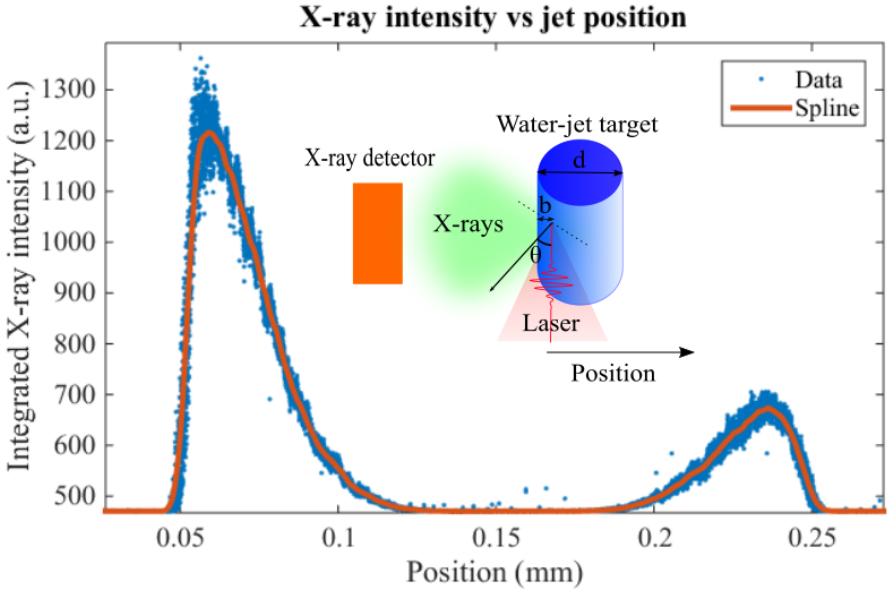

Figure 7: Cross-sectional laser scan over the water-jet displaying x-ray intensity vs water-jet position.

The pointing stability of the focal point can be compared to the size of the laser spot size. If any movement is comparable to the spot size it could be of concern for shot to shot x-ray fluctuations and thus the stability of the source.

1.2 Project's aim

The aim of this project is to determine the stability of the LPXS and normalize with respect to external sources of variation. A basic theory describing the important parameters affecting the x-ray generation has been presented. Obtaining a reproducible x-ray spectrum from each consecutive pulse generated by the LPXS is important for its research applications. The linear regime in the generated x-ray spectrum needs to be constant with each generated pulse. Controlled laser pulse parameters are essential for a stable generation of the x-ray spectrum. Relevant laser pulse parameters will be investigated prior to shot to shot x-ray stability measurements which will reveal the stability of the LPXS.

2 Method

A detailed description of the LPXS setup will be given in this section. In figure 8 an overview of the LPXS setup can be seen. In order to measure the stability of the LPXS the setup was configured for laser shot to shot measurements to determine the spectrum and x-ray flux of individual pulses.

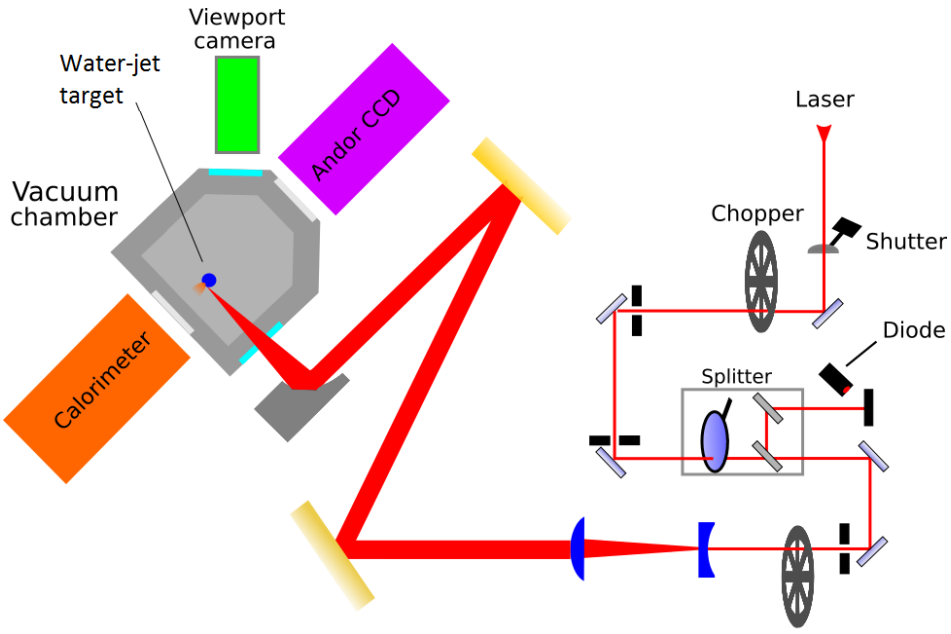

Figure 8: Laser setup overview with vacuum chamber.

2.1 Laser system and optical table setup

In order to generate a laser pulse with the characteristics necessary for the LPXS to work a Ti:Sapphire laser system is used. This system is built by "Spectra Physics" and is based on a short pulse Kerr lens modelocked Ti:sapphire "Maitai" oscillator.

Increasing the pulse to sufficiently high intensity for the LPXS without damaging its internal optics is done using a technique called Chirped Pulse Amplification (CPA). CPA stretches the pulse in time decreasing the peak intensity. The stretched pulse is then passed through a regenerative amplifier before eventual recompression. In this way femtosecond pulses of very high intensity can be achieved[14]. The final pulse generated from our laser system has a total energy of about 6 mJ, with duration ≈35 fs at ≈800 nm and a repetition frequency of 1 kHz. The pre-pulse to pulse ratio should not exceed 1:1000 in optimal working conditions. The laser pulses are directed with a few mirrors on to an optical setup configured for the LPXS as seen in figure 8. In preparation for the shot to shot stability measurements the laser table setup was configured for low repetition rate mode. To decrease the laser pulse frequency from 1 kHz to 2.5 Hz a synchronized double chopper setup was constructed. The low repetition rate was necessary for an Andor CCD camera (which essentially serves as a multi x-ray photon spectrometer, greater details are given in section 2.3) to process and measure the energy of the captured x-ray photons between x-ray shots. As seen in the overview in figure 8 two choppers were used, the first chopper, directly in sync with the laser system, was set

to reduce the laser repetition rate to 50 Hz. A diode was placed to capture the pulses by the beam dump and send a signal to an Arduino unit. The Arduino unit is an open-source electronic prototyping platform which can easily be programmed to interact with electronics. It was programmed to process the signal and generate a sequence of 20 step pulses. These were sent to a stepper motor driver which generated a driving signal to a second chopper. Since there were 400 steps on the second chopper 20 laser shots were needed in order to complete a rotation, thus the repetition frequency could be reduced to 2.5 Hz. In order to correct for any phase difference an additional button was added. Each time the button was pressed an additional step was added to the sequence. A potentiometer was added to adjust the trigger level. Problems were encountered when triggering from the diode, due to the short pulse duration the Arduino did not trigger. A capacitor was added to increase the trigger pulse duration, this was later replaced by a delay generator in order to create a more stable trigger pulse with a steeper leading edge. The chopper synchronization was tested and proved to work successfully for a full day operation. The polarization is adjusted through a rotatable half wave plate before splitting into horizontal and vertical components by a Brewster type polarizer. The transmitted horizontally polarized beam is used for the x-ray generation whereas the s-polarized beam is dumped which will be used for future pump probe experiments. The horizontally polarized beam is sent through a beam expander and directed using two gold mirrors on to a 90 degree off-axis parabolic mirror. The laser is then focused through a window onto the water-jet target held inside a vacuum chamber as seen in figure 8.

2.2 Target

Many different targets for LPXS have been investigated throughout the years, examples of such targets are solid moving wire, metal disc to liquid gallium targets as well as water-jet targets[3, 2]. For simplicity and convenience a water target is used in our experiments. The lower Z density compared to metallic target reduces the x-ray yield from bremsstrahlung, but experiments show only an order of magnitude difference compared to similar setups using high Z targets[6]. Using a water-jet reduces the adverse effects of debris within the source enclosure compared to metallic targets[11]. Due to its self regenerating stable water surface and non-toxicity makes this target material a good candidate for x-ray generation.

2.2.1 Water-jet

The water for a flowing water-jet target is supplied from an impeller pump placed in a water reservoir as seen in figure 10. The pump forces the water through a hose into a copper tubing connected to the baseplate of the vacuum chamber. The water is forced through a $\approx$200 μm inner diameter syringe nozzle creating a smooth water-jet. It flows freely through the laser path about 2 mm below the nozzle down to a catcher tube where the water is recycled back into the water reservoir. When the laser pulse interacts with the water surface a part of the jet is vaporized, this vaporization creates a gap in the stream which extends with a gap-extension velocity. Figure 9 show the laser focused onto the water-jet. The water needs to have enough time to regenerate before the next pulse arrives. This depends on the laser repe-

tition frequency and the water-jet velocity and the distance from the nozzle. Due to the turbulent behavior at high water velocities small perturbations created when the water leaves the nozzle will be amplified by the capillary forces and will eventually result in the water-jet decaying into droplets. The propagation of these surface waves are important for the stability of the water-jet at the point of laser interaction. The characteristic decay length L is given from the Reyleigh-theory[5],

$$L \approx 3v_{jet}\sqrt{\frac{\rho d^3}{\sigma}}. \tag{2.6}$$

Here d is the jet diameter after leaving the nozzle, ρ the density and v_{jet} the water-jet velocity. The jet diameter depends on the contraction factor σ, which in turn is dependent on the type of nozzle. At the time of writing a syringe nozzle is used, but a future setup has been constructed with a pinhole nozzle. The pinhole nozzle will have greater coefficient of contraction but will be easier to replace. A Borda mouthpiece could be used to compensate for the lower coefficient of contraction[18]. In order to pass this criteria the jet apparatus is operated at a flow velocity of ≈5 m/s[5]. A greater jet diameter will increase the laser pointing target area which could decrease the effects of the laser pointing fluctuations, and also increase the stability of the water surface by reducing the effects from the surface tension. However, the increased diameter will require a larger water flow rate which in turn increases the water debris in the chamber. To decrease water debris in the chamber an extended catcher tube was created surrounding the jet with holes for laser and x-ray output. Water vapor and droplets will be force down due to the partial pressure into the catcher tube instead of entering the chamber and potentially condensing on the laser window.

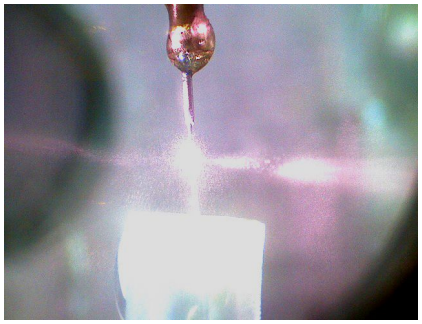

Figure 9: Laser beam focused onto the water-jet inside the vacuum chamber.

2.2.2 Vacuum considerations

To enable production of x-rays the target is maintained within a vacuum environment. A lower pressure reduces the effects of self focusing and enhances the transmission of soft x-rays. The water-jet is therefore in an atmosphere close to the vapor pressure around 15-30 mBar. The vacuum was initially achieved using a 4-staged diaphragm pump with a pumping speed of 0.7 m^3/h combined with a dehumidifier filled with silica gel. While in use the silica gel required constant replacement due to the direct connection with the water reservoir, other problems were encountered such as leaks in the vacuum system. A full reconstruction of the system was therefore justified, the reconstructed system can be seen in figure 10. The old tubing was replaced with high

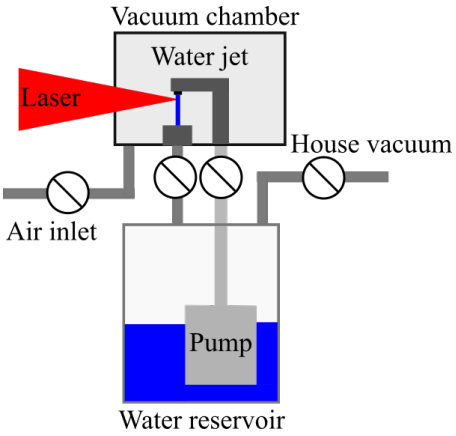

Figure 10: Vacuum system.

pressure hose tubing and valves were added in between each component such that leaks could be identified. It was decided to use the house vacuum which could achieve sufficiently low pressure for our experiments as well as handle the water vapor. The house vacuum was connected with a valve to the water reservoir. The water reservoir is in turn connected through the water catcher tube to the chamber as seen in figure 10. Full day pressure measurement show significant pressure fluctuations which could cause problems for the x-ray generation, see figure 11.

These fluctuations are caused by other users using the same house vacuum line in parallel. The stability of the house vacuum pressure was therefore deemed as insufficient and would only be used until a proper dehumidifier system was obtained. A vacuum chamber was designed and constructed with 1 cm thick aluminum walls to providing sufficient shielding to stop possible electron beams emitted from the source without creating significant bremsstrahlung. The chamber consists of a baseplate and an upper chamber with 6 ports in the cross sectional geometry seen in figure 8. The water-jet system including a copper water inlet, catcher tube water outlet, chamber venting hose and a LED light source all built into the baseplate. The baseplate and chamber cavity were designed to be easily separable for quick adjustments. These are separated by a rubber gasket and are held together by the vacuum pressure. At the time of writing only four ports are used in the configuration seen in figure 8, a laser input window, two $\approx$ 5 μm beryllium windows for the calorimeter and the Andor CCD camera as well as a viewport combined with a camera connected to a computer. More ports might be used for time resolved x-ray spectroscopy measurements[5]. The chamber with water-jet is placed on a movable x-y translation stage allowing micrometer precision when bringing the water-jet into the laser focus.

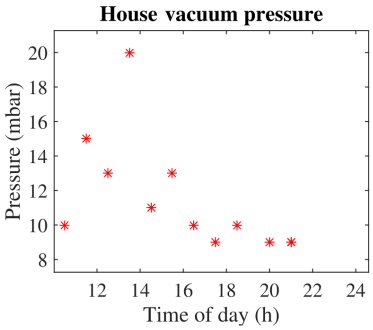

Figure 11: House vacuum pressure fluctuations.

2.3 Detectors: The TES microcalorimeter and the x-ray CCD camera

When the laser has been focused after careful positioning using the translation stage onto the water-jet, x-rays can be generated. The x-ray detectors used for the LPXS must be capable of capturing a full spectrum from each x-ray pulse. In our case two types of energy dispersive detectors are used which are capable of achieving this. A front illuminated x-ray Charge-Coupled Device (CCD) within a Andor-Newton housing used for setup and control and a Superconducting Transition Edge Sensors (TES) microcalorimeter. The TES microcalorimeter is a state of the art calorimetric measuring device capable of reaching an energy resolution of $\Delta E \leq \approx 5$ eV using the steep superconducting transition edge. The TES array is the key to efficient high resolution collection of x-ray spectroscopic data using this LPXS. In its present state of development, effective use of the TES microcalorimeter is technically very demanding. While a working understanding of them has been gained in the course of experiments[22], its

use has been peripheral to the present study. Working descriptions of this remarkable detector system can be found in [5]. Instead the workings of the CCD detector will be described since it will be the main detector used for the shot to shot stability measurements.

The CCD sensor chip is made from a piece of silicon crystal wafer. This wafer has been doped with impurities in order to create a semiconductor layer. The chip is divided into channel rows connected to current-carrying electrodes. These are in turn connected to individual gates on the photo sensitive elements to constitute pixels. Each column of pixels are electrically isolated from each other by insulating barriers[8]. Each pixel is a metal oxide semiconductor capacitor which can store charges when an appropriate bias is placed over the gate, creating a potential well. The reverse bias voltage increases the size of the depletion region in the semiconductor.

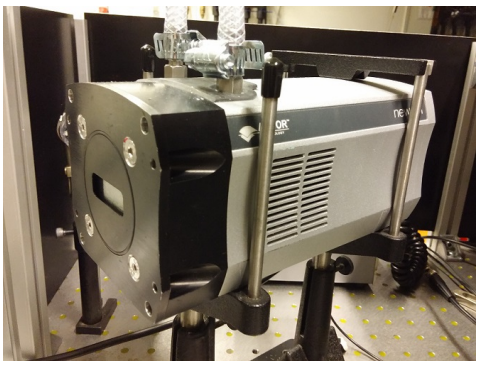

Figure 12: The Andor CCD camera.

When a photon interacts with energy higher than the silicon band gap energy of 1.1 eV an electron-hole pair will form. These electrons are collected in the potential well[8]. If as in our case we have a photon of significantly higher energy than the bandgap, the energy will disperse through multiple photon-electron events, forming a charge-cloud of electrons within the depletion region. The amount of accumulated charge in a single pixel is then proportional to the incoming photon energy. The latter process can be used to retrieve the photon energy from the x-ray photons from the LPXS. Since we have 256 x 1024 pixels all functioning as energy resolving single photon detectors we can build up a spectrum from a single exposure, corresponding to single shot of the laser. This assumes we only have a single x-ray photon interacting with the pixel before the charge is read out which is usually the case due to a relatively low flux. The x-ray photon charge cloud may extend between pixels in which case the corresponding x-ray photon energy will be divided between multiple pixels. Partial registry might also occur where the charge cloud is partly outside the depletion region and is dissipated instead of being registered which needs to be taking into account. More details regarding the detector linearity and their response to x-rays can be found in references[9, 7]. In order to reduce the thermal noise the CCD chip is mounted on a -60 degrees thermo-electrically cooled plate within an argon atmosphere. This atmosphere is preserved and visible light is blocked from reaching the CCD by a beryllium window which is essentially transparent to the x-rays. This detector can be used to capture the spectrum from single x-ray pulses from the LPXS if synchronized to the laser pulses. The captured images from each shot can be analyzed to determine the shot to shot stability[5].

2.4 Experimental investigation of the external parameters

Some of the relevant parameters affecting the generation of x-rays has been discussed; laser target angle, laser intensity, pulse shape, polarization and focusing parameters. Since the overall stability of the LPXS is a function of the stability of these parameters it was of interest to determine the magnitude of the separate parameter fluctuations. Before the shot to shot stability measurements, two parameters namely the laser pointing and laser pulse energy fluctuations were investigated. These were chosen since they have been judged as main contributors to the x-ray fluctuations in a similar LPXS[11]. In order to capture data regarding the laser pulse, a beam profile sensor was used. This sensor captures the laser beam cross-sectional profile both horizontally and vertically on a sensor array. Both laser beam position and light intensity can be determined for each single pulse using this detector.

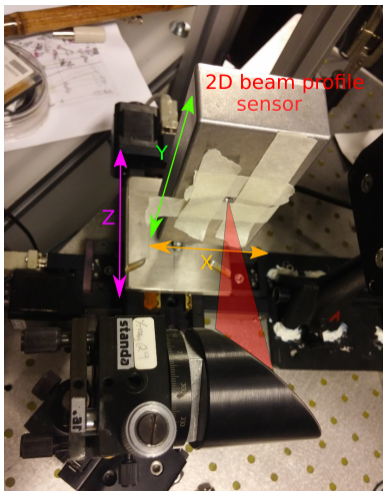

(a) Beam profiler placed in alignment with the laser focal point.

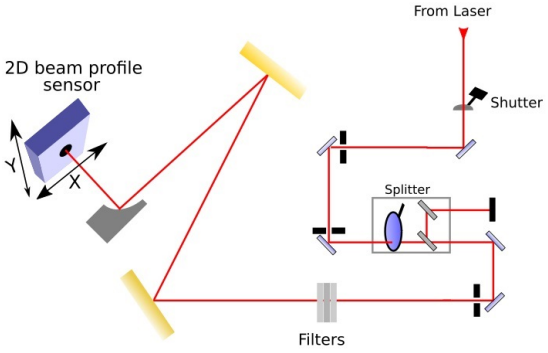

(b) Laser setup overview with beam profiler.

Figure 13: Laser stability measurements.

The 2D beam profile sensor with 256x256 pixels on a 2x2 mm sensor was mounted on the x-y translation-stage steerer in place of the vacuum chamber (see figure 13 and compare with figure 8). It was synchronized with the laser system to capture the profile of each individual laser pulse at a pulse repetition frequency of 1 kHz. The full ≈6 W at 1 kHz pulsed laser beam was available at the laser table but was reduced in intensity with a variable beam splitter to about 70 mW. Further reduction in intensity was achieved with a combination of 3 filters with OD 3, 2 and 2 (see figure 13b). Since a measurement of the absolute value of the peak intensity was not of interest the intensity was reduced to an unknown value below the saturation threshold of the sensor. It was moved horizontally (x) using the translation-stage and manually moved vertically (y) with respect to the laser table until the beam was centered on the sensor (see figure 13b). Due to damage on the filters the filter configuration was moved until the profile shape was free from artifacts and back reflections. The profiler was gradually adjusted along the z-direction towards the focal spot to the point where it was close enough to avoid saturation.

The measurements were done by capturing bursts of 3000 laser pulses at 1 kHz (1 ms per pulse), combined with 10 second dead time proceeded by another 3 second burst. Data for each pulse was saved in a 256+256 data point array containing information of horizontal and vertical beam profile. Two experiments were preformed; one with and one without the use of laser table covers. These covers are mainly used for safety reasons in order to protect the user from the laser but also protects the beam path from external influences such as air currents. The two measurements were performed over 80 minutes. These were proceeded by an additional 8 hour long-term measurement with table covers on. The beam profiler was placed at different locations from the point source in order to observe longitudinal fluctuations (along z-direction) in the beam path. Unfortunately the beam profiler was saturated and these experiments could not proceed.

2.5 Shot to shot stability measurements

After performing the laser stability measurements the laser table was configured according to figure 8 and prepared for the shot to shot stability measurements. The system was configured for optimal x-ray generation through careful mirror adjustments and focusing. During pump-down procedure the pressure in the chamber reached 40 mBar, however, bubbles were observed in the tube connecting the water-jet to the water pump. This resulted in an unstable water-jet, the vacuum system needed resealing. After sealing a leak in the water hose connecting the water reservoir to the vacuum chamber, see figure 10, the water-jet was stabilized. After careful positioning of the laser onto the water-jet using the translation-stage steerer a few x-ray photons were observed on the Andor CCD camera. The low x-ray flux observed on the Andor CCD was insufficient for the experiment to proceed. The laser pulse spectrum was later analyzed using a spectrometer and it turned out to be strongly asymmetric. The laser system was not functioning properly and could not be fixed within the time of this project. It is believed that this was the cause for the low x-ray yield which impaired the shot to shot stability measurements.

2.6 Post processing

The sensor used for investigating the laser stability captures the beam cross-sectional profile both horizontally and vertically as seen in figure 14. Both laser spot position and pulse energy can be determined for single laser pulses using this detector. In the coming section the procedure used to determine these two quantities will be introduced. Furthermore, a method prepared for analyzing x-ray photons captured by the Andor CCD for the shot to shot stability measurement is presented.

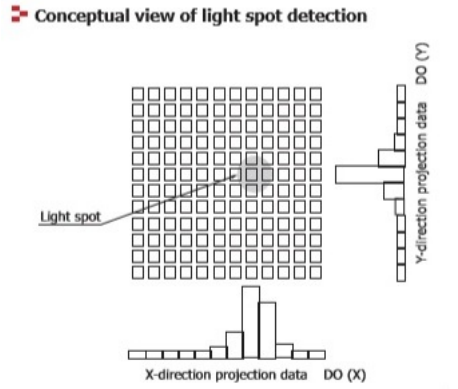

Figure 14: The figure shows the beam profiler and the two profiles created from the laser spot[21].

2.6.1 Beam profiler data

A sample of a horizontal and vertical beam profile captured by the profiler can be seen in figure 15. Smaller peaks could be observed in all profiles along with a main peak, these are not relevant for the task at hand and originate from known artifacts created by defects in the filters. The profile data was therefore cut to focus on the main peak only. Each data point is assumed to have an uncertainty of ±0.5 ADCU (analog to digital converter units).

The purpose was to obtain the peak position to the highest possible accuracy for each single pulse. In the experiment the size of each pixel was 7.8 μm. The initial approach to determine the peak position, was to find the pixel position with the greatest value. This would result in an uncertainty corresponding to the pixel size which turned out to be insufficient. To achieve sub-pixel accuracy an algorithm was employed where the maximum pixel value and the three adjacent values in each direction were chosen. The seven element vector of peak values was fitted with different functions such as a Gaussian, Laurentian, hyperbolic secant, pseudo voigt and a polynomial. A Gaussian fit was chosen since no other fit showed any noticeable difference in accuracy, see figure 15. The peak vector containing the seven peak values was therefore fitted with a Gaussian with the free parameters A,b and c with a constant noise background B set manually,

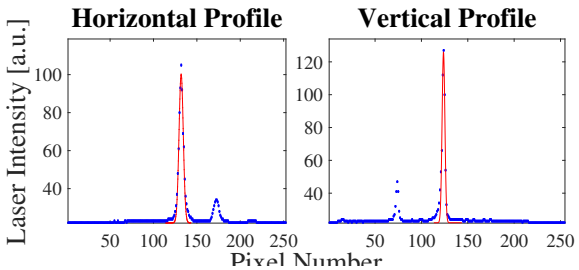

Figure 15: Horizontal and vertical beam profile data.

$$g(x) = Ae^{\frac{-(X-b)^2}{2c^2}} + B.$$

The fitting was done using the Matlab 2014b fit function tool which performs a nonlinear least square fit to determine the parameters[27]. Samples of fitted profiles can be seen in figure 16. The peak position was determined from the constant b obtained from the fit which describes the central position of the Gaussian. In order to estimate the uncertainty the asymptotic linearized confidence interval was obtained for the parameters determined from the fit[28]. Using a confidence level of 0.68% an approximation to one standard deviation was obtained[25], more information about the estimation of errors in nonlinear fits can be found in the reference [26]. The main peak position and its uncertainty could then be determined for both profiles. The total pulse energy was obtained by summing the data values for each peak profile and subtracting the back-

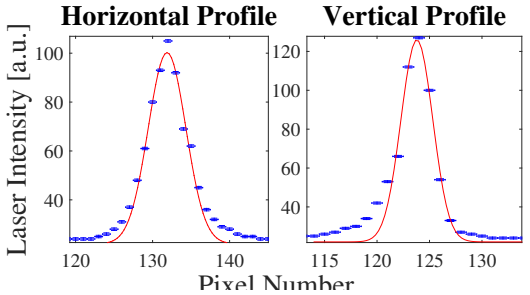

Figure 16: Gaussan fit to the main peak for the two profiles.

ground B. Since the uncertainty was $\pm$ 0.5 ADCU for each value the total uncertainty is given by the error summed in quadrature. The total uncertainty is the root of the number of values times the uncertainty for each value $0.5 \cdot \sqrt{256} = 8$. For the long-term measurements the average value of several pulses was calculated from each burst. Additionlly the standard error of the average was calculated using,

$$SE_{average} = SE_n/\sqrt{N}$$

where N is the number of samples used in the average and SE_n is the standard error of each sample[30].

2.6.2 X-ray CCD image processing

A program was created to analyze the images from the x-ray detecting Andor CCD for the shot to shot stability measurements. The initial procedure in the image processing was to remove the thermal noise. The image was converted from a uint16 bit format to integer values in a 2D matrix. The matrix was then converted into a histogram where a Gaussian distribution was fitted to the thermal noise. All values below the higher end, 5 sigma width, of the fitted peak were removed from the histogram. The non-zero pixel elements in the image, now without thermal background were identified and adjacent pixel elements were added to account for multi-pixel events. The spectrum could then be calibrated using K_α and K_β x-rays from an iron-55 calibration source by splining the histogram and fitting the peaks to the corresponding values.

3 Results and discussion

The results from the experimental investigation of the external parameters is presented. Both the laser pointing and pulse energy fluctuations are determined and the impact of these parameters on the LPXS stability are discussed.

3.1 Laser pointing fluctuations

The temporal development of laser position over 3 seconds, corresponding to 3000 pulses, can be seen in figure 17a for both peak profiles. Oscillatory behavior can be observed. The oscillation amplitudes are in the order of 0.3 pixels, corresponding to 2.3 μm for horizontal movements while slightly lower for vertical. With the used algorithm a sub-pixel accuracy of about one forth of a pixel width was achieved, which is less than 2 μm. Despite the increased accuracy using the algorithm the error is comparable to the magnitude of the fluctuations. The long-term measurement containing 80 min worth of data (using 30 pulse average per burst) can be seen in figure 17b.

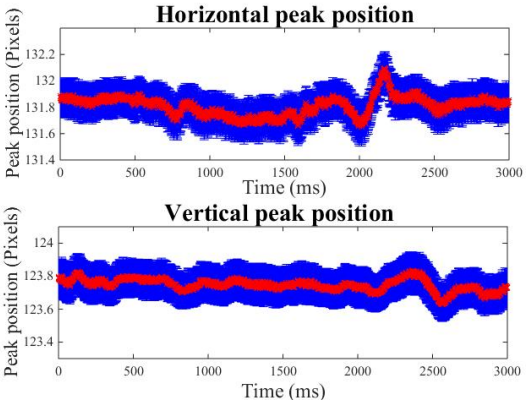

(a) 3000 ms burst sample.

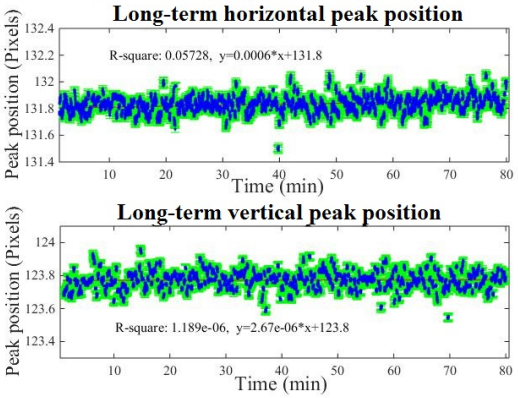

(b) 80 min 30 pulse averaged long-term measurement.

Figure 17: Short and long-term laser pointing fluctuation measurements.

By averaging the pulses, the error reduced to the standard error of the mean for the 30 pulses analyzed. A linear function was fitted to the long-term measurements. Aside from a very weak positive slope in the linear regression, no clear drift or low frequency oscillations could be observed in the long-term measurements. This weak slope is within the expected uncertainty. Small long-term movements could be explained by the heating of the optics due to thermal expansion. Any thermal expansion, however, would most likely reach thermal equilibrium within the time of measurement.

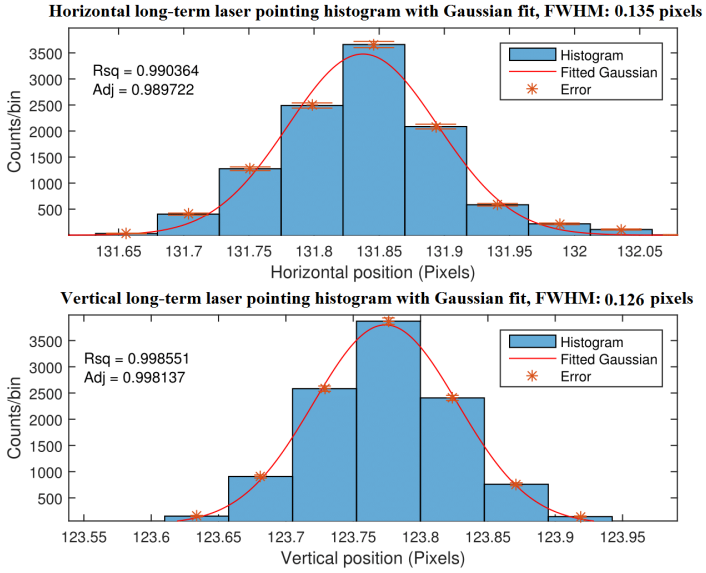

Figure 18: Peak position distribution for long-term measurements.

The long-term 30 pulse averaged pointing position is presented in a histogram for both vertical and horizontal beam profile, see figure 18. The position distribution was fitted with a Gaussian function. This normal distribution indicates a FWHM of 0.135 pixels horizontally, corresponding to 1.05 μm, and vertically 0.126 pixels, corresponding to 0.98 μm. These fluctuation amplitudes are smaller albeit comparable to the size of the laser focal spot which was estimated to about 2 μm as described in section 1.1.3. The horizontal movement is slightly larger than the vertical movements although both show a fluctuation amplitude of about 1 μm FWHM. In the beginning of this paper we emphasized the importance of the angle of incidence onto the target with respect to the x-ray generation from the LPXS. Any laser movement along the vertical axis will result in little to no x-ray variations due to the symmetry along the length of the water-jet. On the other hand the horizontal pointing movement will subsequently lead to a greater influence of the x-ray generation. We can estimate the fluctuation in the x-ray yield from the observed horizontal laser pointing fluctuation. This is done by comparing with the data from the cross-sectional laser scan over the water-jet, see figure 7. Assuming an initial laser position yielding maximum x-ray generation (the peak of the x-ray intensity to position plot), the significance of horizontal fluctuations on x-ray intensity can be determined, see figure 19. This correlation shows that the observed laser pointing fluctuation of about 1 μm have little influence to the x-ray intensity. However, when the laser moves further away from the peak of maximum intensity towards a greater angle of incidence we reach a steep slope. The greater derivative in this region will increase the influence of pointing fluctuations to the x-ray intensity dras-

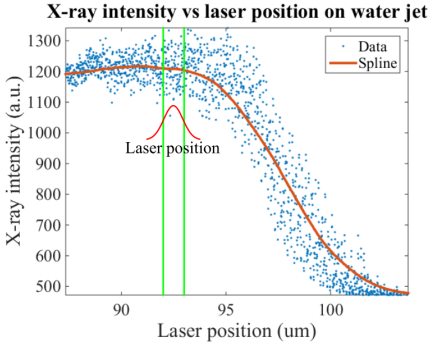

Figure 19: Correlating beam scan data for x-ray intensity in figure 18 to pointing position distribution in order to estimate the x-ray fluctuations.

tically. This stresses the importance of finding the point of maximum x-ray intensity before performing experiments using the LPXS. How this pointing variation influences the spectrum shape remains unknown until shot to shot measurements are performed.

In order to determine the origin of the fluctuations the frequency domain was analyzed, see figure 20. The lower frequency oscillations observed in figure 17a are represented by peaks in the frequency spectrum. Two double peaks are clearly seen both vertically and horizontally at the frequencies 36, 37 Hz and 62, 64 Hz. The horizontal fluctuations are dominated by two major frequencies, 37 and 62 Hz, while the main frequencies in the vertical measurements are around 36 and 64 Hz. The general observation is that the oscillations of greatest amplitude have a frequency around 64 Hz combined with a peak of slightly lower amplitude around 36 Hz.

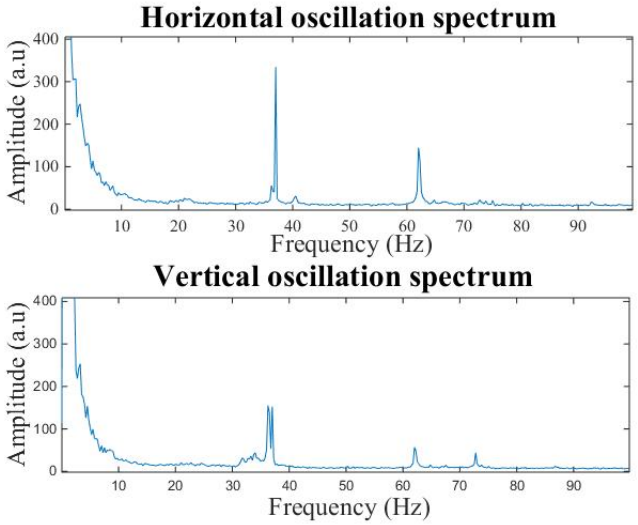

Figure 20: Frequency analyzed pointing fluctuations. The horizontal pointing distribution is superimposed at the point of maximum x-ray intensity. The in order to compare to the determined in is superimposed green lines indicate the FWHM width.

The origin of the peaks in the frequency domain is speculative, since these frequencies do not correspond to known aspects of the laser, the choppers or other external apparatus in the lab. The two experiments with and without laser table covers showed no significant difference. The ventilation system is therefore not believed to be of concern for the laser pointing stability. Accelerometers were placed on the laser table to identify any physical vibrations believed to be the origin of the peaks observed in the frequency domain. Vibrations on the laser table were observed at frequencies mainly below 25 Hz including smaller amplitudes at the mains frequencies 50, 100 and their harmonics at 200 Hz; these measurements can be seen in appendix A. There are no particular frequencies in the pointing measurement that can be attributed to any table vibrations based on these measurements. The origin of the vibrations could be caused within the laser system which remains unknown. Further analysis is needed in order to determine the origin of the laser pointing fluctuations, however, we expect a low influence to the x-ray yield thus it should not be of great concern for our LPXS.

3.2 Laser pulse energy fluctuations

The short-term laser energy fluctuations for a burst containing 3000 pulses is seen in figure 21a and long-term 80 min measurement is seen in figure 21b. A weak drift is indicated with the linear fit in the long-term measurements, during these 80 minutes the intensity dropped by about 0.5%. A possible reason for this drift could be that the laser interacting with the components inside the laser system or on the laser table. Heating of optical elements could result in a changed absorption, as previously discussed thermal equilibrium should be reached in the timescale of the measurements. Alternatively, the sensor may have become fatigued due to the long-term laser exposure; this remains to be verified.

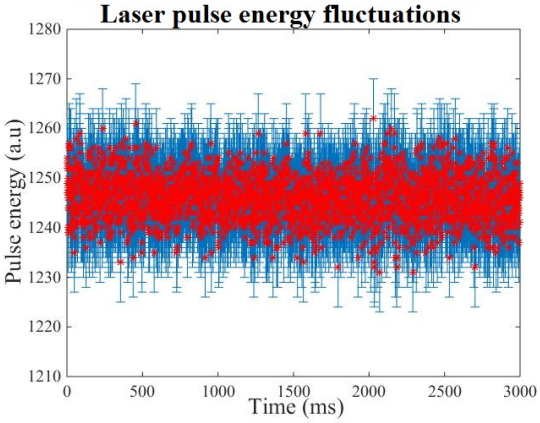

(a) 3000 ms burst sample.

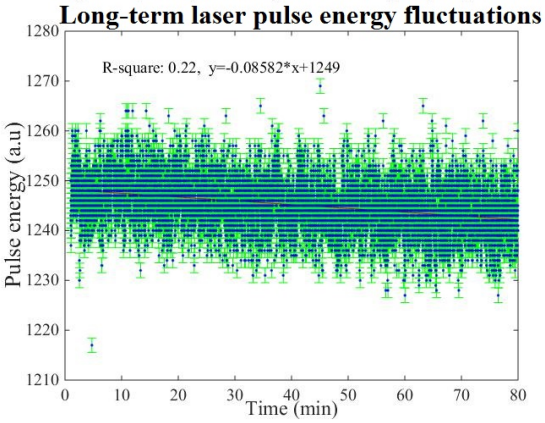

(b) 80 min long-term measurement with 30 pulse average.

Figure 21: Short and long-term laser pulse energy fluctuation measurements.

The short-term pulse energies are presented in the histogram in figure 22. The histogram was fitted with a Gaussian distribution which indicated a FWHM of 13.7 a.u. at the average pulse energy of 1280 a.u. which corresponds to approximately 1.07% pulse to pulse energy fluctuations. This can be compared to the specifications of the laser system used. According to the manufacturer the pulse to pulse variations should be below 1%.

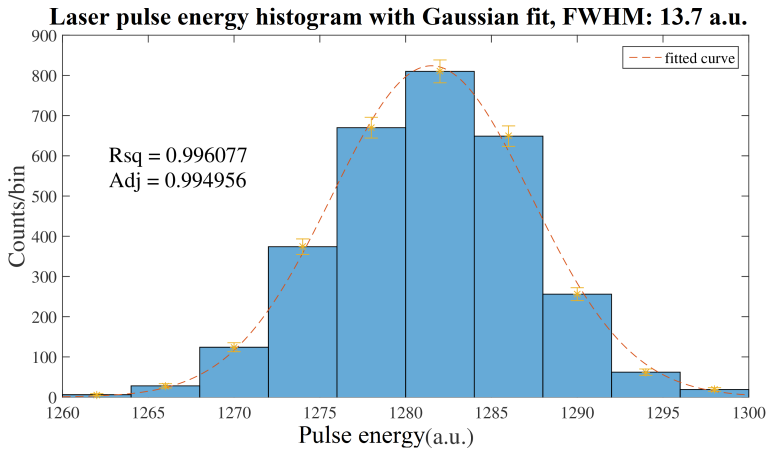

Figure 22: Laser pulse energy distribution for single burst measurement.

The frequency analyzed laser energy measurements seen in figure 23 reveal multiple dominant frequencies. These frequencies are represented by peaks in the frequency domain. To verify that the origin is not caused by noise the spectrum was compared to the sensor background spectrum in figure 24. Interestingly a symmetry is seen at 375 Hz which indicates a Nyquist frequency lower than the expected 500 Hz which is half of the sampling frequency of 1 kHz. This leads to suspicions regarding the accuracy of the technique. Many of the peaks can be attributed to the background noise from the data collection.

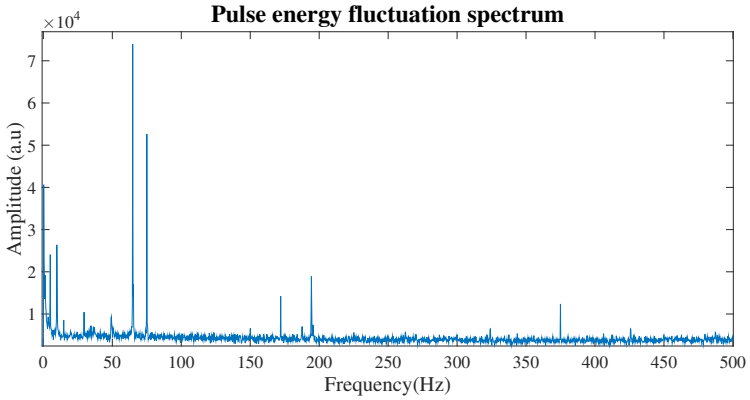

Figure 23: Frequency analyzed laser pulse energy fluctuations.

One interesting peak is seen at 64 Hz for both measurements which cannot be explained by the background noise. It is likely that the pulse energy fluctuations are coupled to physical vibrations. Corresponding peaks are also seen at 64 Hz for the pointing stability measurements, see figure 20. An increased beam path and vibrations within the cavity could be a source for laser pulse fluctuations. Further investigation is required in order to deduce the origin of these fluctuations. Since most peaks can be attributed to the background noise from the detector itself, it is likely that the actual laser pulse energy fluctuations is lower than the 1% which was previously determined.

The laser pulse energy fluctuations cannot easily be correlated to the variations in x-ray generation since intensity is dependent of both area and energy. However, if we assume that the longitudinal fluctuation of the laser focus is negligible then the pulse energy variations will determine the laser intensity fluctuation. Taylor expanding expression 1.4 with respect to ΔI for small variations simplifies the expression to a linear relation with respect to the hot electron temperature (which determines our x-ray spectrum). Accordingly we expect low hot electron temperature variations of less than 1% caused by the fluctuations in laser pulse energy. Judging from figure 6 we expect very small changes in the generated x-ray spectrum between shots.

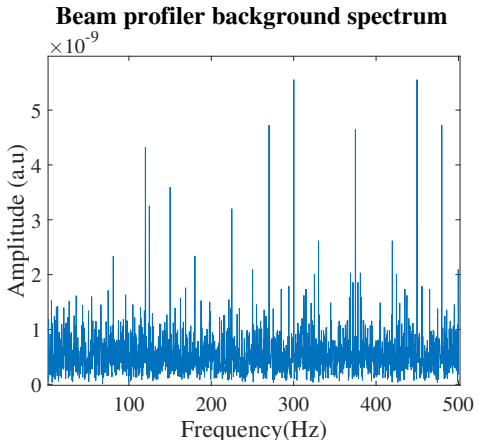

Figure 24: Background beam profiler spectrum.

4 Outlook

Due to problems with the LPXS setup it was not possible to achieve conditions with satisfactory x-ray production to perform the shot to shot stability measurements within the time span of this project. Nevertheless, the LPXS has been prepared for these future measurements which will reveal the true significance of how much the separate variable fluctuations will affect the stability of the LPXS. Two of the variables affecting the x-ray generation has successfully been determined. Based on the results we expect low fluctuation in the x-ray yield and spectrum between shots.

The LPXS is complex and is dependent on the simultaneous function of many variables many of which remains to be investigated. For example, the pointing stability along the longitudinal (z) direction, see figure 13 in section 2.4. An experiment was prepared where the beam profile was captured at distances before and after the focal point with the intent of investigating this variable. Unfortunately the sensor was broken and the experiment could not proceed further. The width of the beam profile captured by the sensor could then be used to determine the longitudinal position using the calibration curve. The focal point position could be determined in 3D for each pulse, which could be used for improving the understanding of the laser pointing stability. Another future investigation is to determine water-jet surface instabilities. Experiments could be performed by observing the water surface reflection of a defined laser beam through a pinhole. The fluctuations of the reflected

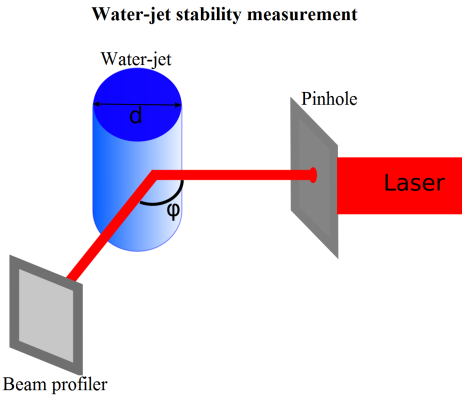

Figure 25: Measuring the water surface fluctuations.

beam could be observed using the beam profiler as seen in figure 25. Investigating the temporal pulse shape such as leading edge, pulse width and pre-pulse fluctuations could be performed using an oscilloscope and an ultrafast diode. The pulse shape is essential for the x-ray generation and turned out to be the main reason for the lack of x-rays in the shot to shot stability experiment. The underlying reason for investigating the shot to shot x-ray variations is to determine whether the spectrum shape changes significantly between pulses. As seen in figure 6 even with a very large variation in laser pulse energy the spectrum shape remained intact, small variations of a few percent seen from the results will likely not be of great concern for the LPXS setup. The future shot to shot measurements will reveal the true significance of the variable fluctuations determined in this investigation. If the shot to shot measurement reveal greater spectrum variation than what the external parameter investigation predict then further steps could be taken to investigate the origin of the instabilities.

5 Conclusions

The goal of this investigation sought to determine the overall stability of the LPXS and normalize with respect to external sources of variation. A LPXS setup was constructed to measure the x-ray spectrum and flux in single pulsed mode to determine the stability of the LPXS. Due to problems with the laser system it was not possible to achieve conditions with sufficient x-rays to perform these experiments. External sources which influences the conditions for x-ray generation, such as the laser pointing stability and laser pulse energy fluctuations, were investigated using a laser beam profiler. By capturing multiple pulses and determining the peak position using peak finding algorithms the pointing fluctuation for long-term 80 min measurement could be determined to approximately 1 μm from the FWHM of the normal distribution curve. The used method could verify a short-term pulse to pulse energy fluctuation of less than 1% while long-term measurements showed a drift of 0.5% pulse energy decrease after 80 min. The low fluctuation observed in both laser pulse energy and pointing stability is not expected to be of concern for the stability of the LPXS. Future x-ray shot to shot measurements will reveal the significance of these fluctuations. In short, the investigation has resulted in valuable knowledge of sources affecting the LPXS stability and the construction of a setup capable of performing single shot to shot stability measurements for the LPXS, which will be used to determine the stability of the LPXS.

Acknowledgements

I would like to thank my supervisors Jens Uhlig and Amal El Nahhas for the support they have provided throughout the project and Wilfred Fullagar for his help and contribution.

A Appendix: Laser table vibration spectrum

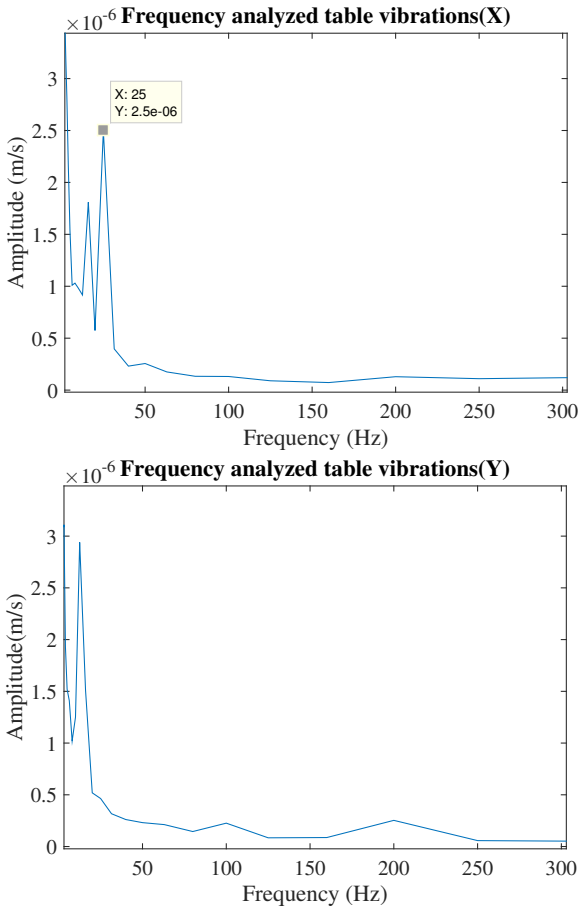

Figure 26: Frequency analyzed laser table vibrations.

B Appendix: Vacuum heating theory comparison to experiment

The cross-sectional laser scan over the water-jet measuring the x-ray intensity can be compared to the theoretical model for the vacuum heating process in order to verify the accuracy of the presented model. Equation 1.3 describing the vacuum heating was solved numerically and converted as a function of angle to position on the water-jet using equation 1.5. The function was convoluted with a Gaussian of 4 μm FWHM corresponding to an approximate beam cross-section at the focal point. The data in figure 7 was then normalized and compared to the theory with respect to the unattenuated x-ray intensity peak. Figure 27 show the solution with $C = 1.15$ and $a = 0.55$ compared to the experimental data. Here we assume that the x-ray generation is proportional to the absorption into vacuum heating. The jet scan was performed with a laser pulse energy of 3 mJ corresponding to $a \approx 0.7$ not including losses at the laser table. A value of $a = 0.55$ is reasonable considering the loss in intensity when the pulse reaches the target, here the greater beam projection area on the water surface will result in further lowering the intensity. The absorption factor C was set to $C = 1.15$ which corresponds to a 13% loss in intensity through other processes than vacuum heating. The reflected beam intensity could be measured and compared to the initial beam intensity and light scattering in future experiments to verify whether this was is good estimate. The theoretical model show an angle of maximum absorption at 84.5 degrees for these values.

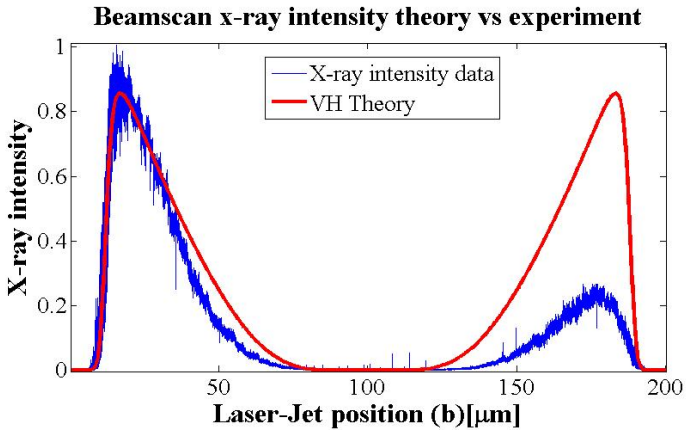

Figure 27: Theoretical VH model fitted to the experimental beam scan data. The theory show a maximum absorption at 84.5 degrees with $a = 0.55$ and $C = 1.15$ Theoretical fit to experimental data.

The theory deviates from the experimental results at the shallower slope corresponding to lower angle of incidence. This could be a result of inaccuracies in the model used. At the lower angles the electric field component perpendicular to the surface is decreased. Vacuum heating assumes that the electrons are pulled out beyond the resonant regime around the critical plasma density[3]. The resonant absorption process might be more applicable in this regime for lower angles due to the lower electric field component perpendicular to the surface. This absorption process absorbs less energy than the vacuum heating mechanism which could describe the lower x-ray yield com-

pared to the model used[17]. Combining the two models for separate regimes could be done and compared to the experimental data to verify if this is indeed the case. Furthermore the water-jet diameter was not measured accurately and it was also assumed that the water-jet had a perfect cylindrical cross section, understanding the water-jet shape is important to proceed further with the analysis. The values could be fitted to the beam scan data with a least square fitting algorithm to determine the values of a and C, assuming the theory is valid. This comparison indicates that the vacuum heating theory described in this paper can likely be used to describe the x-ray generation from the LPXS at the greater angle of incidence to the target. Further research is needed in order to verify the generality of these claims.

C References

References

[1] GIBBON, Paul. Short pulse laser interactions with matter. World Scientific Publishing Company, 2004.

[2] SJÖGREN, Anders. Laser-matter Interactions at Extreme Irradiance: x-ray Generation and Relativistic Channelling. Lund University, 2002.

[3] THOß, Andreas. x-ray emission and particle acceleration from a liquid jet target using a 1-kHz ultrafast laser system. 2003. PhD Thesis. Freie Universität Berlin, Germany.

[4] GENOUD, Guillaume. Laser-Driven Plasma Waves for Particle Acceleration and x-ray Production. Lund University, 2011.

[5] UHLIG, Jens. Life of a photon in x-ray spectroscopy. Lund University, 2011.

[6] FULLAGAR, Wilfred, et al. A broadband laser plasma x-ray source for application in ultrafast chemical structure dynamics. Review of Scientific Instruments, 2007, 78.11: 115105.

[7] UHLIG, Jens, et al. Laser generated 300 keV electron beams from water. Laser and Particle Beams-Pulse Power and High Energy Densities, 2011, 29.4: 415.

[8] JANESICK, James R. Scientific charge-coupled devices. Bellingham: SPIE press, 2001.

[9] FULLAGAR, Wilfred, et al. The use and characterization of a backilluminated charge-coupled device in investigations of pulsed x-ray and radiation sources. Review of scientific instruments, 2008, 79.10: 103302.

[10] TEICH, MALVIN CARL; SALEH, B. E. A. Fundamentals of photonics. Canada, Wiley Interscience, 1991, 3.

[11] MIAJA-AVILA, L., et al. Laser plasma x-ray source for ultrafast time-resolved x-ray absorption spectroscopy. Structural Dynamics, 2015, 2.2: 024301.

[12] ASSMUS, Alexi. "Early history of X rays." Beam Line 25.2 (1995): 10-24.

[13] KONINGSBERGER, D. C., and Roelof Prins. "x-ray absorption: principles, applications, techniques of EXAFS, SEXAFS, and XANES." (1988).

[14] Maine, P., et al. "Generation of ultrahigh peak power pulses by chirped pulse amplification." Quantum electronics, IEEE Journal of 24.2 (1988): 398-403.

[15] CHU, H.-H., et al. A versatile 10-TW laser system with robust passive controls to achieve high stability and spatiotemporal quality. Applied Physics B, 2004, 79.2: 193-201.

[16] MIURA, Eisuke. Electron Acceleration Using an Ultrashort Ultraintense Laser Pulse, Femtosecond-Scale Optics. Prof. Anatoly Andreev (Ed.), ISBN, 978-953.

[17] BRUNEL, F. Not-so-resonant, resonant absorption. Physical Review Letters, 1987, 59.1: 52.

[18] DONG, Wei-guo; LIENHARD, John H. Contraction coefficients for Borda mouthpieces. Journal of fluids engineering, 1986, 1081377.

[19] SHIMAZAKI, Hideaki; SHINOMOTO, Shigeru. A method for selecting the bin size of a time histogram. Neural computation, 2007, 19.6: 1503-1527.

[20] `http://en.wikipedia.org/wiki/Laser_beam_profiler` Accessed 2015-05-09

[21] `http://www.hamamatsu.com/eu/en/product/alpha/P/4213/S9132/index.html` Accessed 2015-06-30

[22] UHLIG, J., et al. High-resolution x-ray emission spectroscopy with transition-edge sensors: present performance and future potential. Journal of Synchrotron Radiation, 2015, 22.3: 766-775.

[23] ALS-NIELSEN, Jens; MCMORROW, Des. Elements of modern x-ray physics. John Wiley & Sons, 2011.

[24] MULSER, Peter; BAUER, Dieter. High Power Laser-Matter Interaction. Springer Science & Business Media, 2010.

[25] CI, Basics Confidence Intervals. Statistical inference. 2009.

[26] BURRELL, Keith H. Error analysis for parameters determined in nonlinear least squares fits. American Journal of Physics, 1990, 58.2: 160-164.

[27] `http://se.mathworks.com/help/curvefit/fit.html;jsessionid=8f7487e890637d8e2b8445d69155` accessed 2015-05-10

[28] COX, Christopher; MA, Guangqin. Asymptotic confidence bands for generalized nonlinear regression models. Biometrics, 1995, 142-150.

[29] L'HUILLIER, Anne, et al. Generation and properties of HHG radiation. 2010.

[30] BLAND, J. Martin; ALTMAN, Douglas G. Statistics notes: measurement error. Bmj, 1996, 313.7059: 744